sustainability

MDPI

Article

A Dual DIC System for Analysis of Dynamic Mechanical Properties of Large Sandstone under Uniaxial Compression Load

Yichen Zhong [1,†], Fanxiu Chen [1,*,†], Xinya Gao [1], Zhanwei Guo [1], Jie Sun [2], Liming Zhang [2], Yuan Wang [1], Yuxin Liu [1] and Changtai Li [3]

[1] School of Science, Qingdao University of Technology, Qingdao 266520, China
[2] School of Civil Engineering, Qingdao University of Technology, Qingdao 266520, China
[3] Shenzhen Haytham Technology Co., Ltd., Shenzhen 518118, China
* Correspondence: mecfx@163.com
† These authors contributed equally to this work.

Abstract: In this paper, an experiment is carried out to acquire the dynamic mechanical properties of a simulated sandstone tunnel by a dual DIC system. The sandstone tunnel is simulated by large sandstone with a prefabricated hole in the center. The speckle size required by DIC system was evaluated, and the results showed that for large specimens a marker pen could be used to spot speckles and make sure that the diameters of speckle points in an image should be ranged from three to five pixels. The dual DIC system is composed of a low-speed camera and a high-speed camera. The low-speed camera is used to record the speckle patterns of the sandstone in one side during the whole process of compression load, and the high-speed camera is placed in the other side to record speckle patterns for 11.5 seconds before and after failure. It is realized that monitoring whole process of deformation and instantaneous failure in two directions is required. Measurement results are effectively analyzed. The results are shown as follows: At the initial stage of loading the sandstone is in an elastic stage without macroscopic cracks. With the increase in compression load the sandstone has several small stress releases and several obvious macroscopic cracks. In the final stage of loading, the distribution of normal stress and shear stress are almost the same, and cracks are subjected to the coupling effect of normal stress and shear stress. The two ends of the prefabricated hole perpendicular to the applied load direction are prone to cracks parallel to the applied load direction.

Keywords: digital image correlation; sandstone tunnel mechanics; crack extension; global strain field; mechanical properties

Citation: Zhong, Y.; Chen, F.; Gao, X.; Guo, Z.; Sun, J.; Zhang, L.; Wang, Y.; Liu, Y.; Li, C. A Dual DIC System for Analysis of Dynamic Mechanical Properties of Large Sandstone under Uniaxial Compression Load. *Sustainability* **2023**, *15*, 2623. https://doi.org/10.3390/su15032623

Academic Editor: Jianjun Ma

Received: 18 December 2022
Revised: 15 January 2023
Accepted: 28 January 2023
Published: 1 February 2023

1. Introduction

Many scholars have worked on the destructive mechanism of circular tunnels [1–3]. Many collapse disasters in tunnel engineering are caused by rock deformation and failure. The essence of rock failure is the dynamic evolution process of crack initiation, expansion and interpenetration under the action of load [4–6]. Scholars have used CT scanning, acoustic emission, scanning electron microscopy and other measurement methods to research the evolution of rock cracks. Among them, Huang [7] conducted triaxial compression experiments on granite samples with two coplanar three-dimensional defects. He found that shear cracks and anti-wing cracks are dominant under high confining pressures. Duan [8] carried out CT scanning on the long maxi shale in the uniaxial compression test and found that the distribution of fine and dispersed minerals has little effect on the final fracture morphology, and the increase in pore ratio is related to fracture volume and failure connectivity mode. Dai [9] used acoustic emission and scanning electron microscopy to study the development of various rock micro-cracks quantitatively. He found that micro-cracks

distribution changes from diffusion to localization as stress increases. Zhao [10] used acoustic emission and scanning electron microscopy in the true triaxial compression tests of the Jinping marble. The results show that the magnitude of the intermediate principal stress and the minimum principal stress affect the brittle ductile transition and failure mechanism of Jinping marble. Gao [11] conducted true triaxial compression tests on 50 mm × 50 mm × 100 mm hard rock (granite, marble and sandstone) and found by scanning electron microscopy that the influence of intermediate principal stress on the strength, deformation and failure was significant. Compared with the above methods, Digital Image Correlation (DIC) has many advantages in deformation observation, such as lower requirement to measurement environment and conditions, high degree of automation, ease of operation, non-contact measurement, full-field information obtained, and high measurement accuracy. In the 1980s, Yamaguchi [12] in Japan and Peters and Ranson [13] in the United States proposed the basic idea of a digital image correlation measurement method for the first time. Due to its full-field, non-contact, high-precision and convenient operation characteristics it has been widely used in many fields [14]. In recent years, scholars have applied this method to the analysis on rock damage and deformation [15,16].

At present, in the selection of tunnel test material size, most scholars choose to use small-size simulation material, and further research is needed on the tunnel simulation test of large-size real rock mass. Based on the similar model test of large sandstone tunnels and the DIC method, it is studied for the evolution law of crack initiation, extension and penetration in rock specimens with prefabricated holes under uniaxial compression in this paper. Under different stress states the strain localization characteristics of specimens are analyzed from the perspective of global strain field. The research results can not only deepen the understanding on rock crack extension mechanism, but also provide a theoretical and data support for design, construction and operation of similar projects.

2. Specimen Preparation and Compression Experimentation

In this paper sandstone, which is a brittle rock, is used as a specimen. The selected standard cylindrical sandstone sample has a uniaxial compressive strength of 43 MPa, elastic modulus of 10.1 GPa, and density of 2120 kg/m^3. The sandstone sample is processed into cuboid specimens of 500 mm × 500 mm × 100 mm (length × width × thickness), and a prefabricated hole with the diameter of 100 mm through the thickness direction is cut by a water knife in the center of the sandstone, as shown in Figure 1.

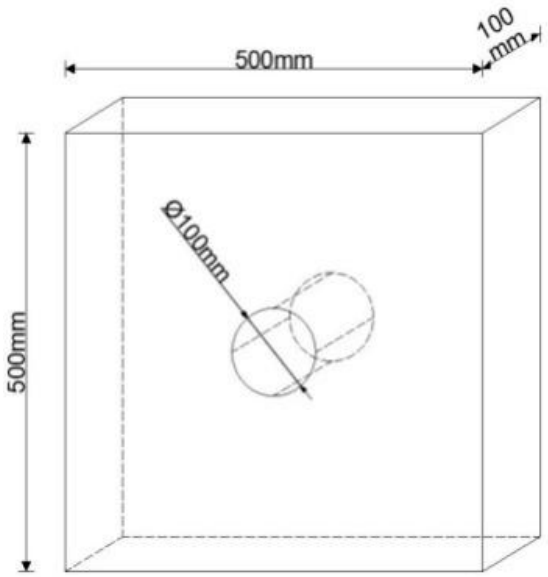

Figure 1. Specimens and prefabricated hole.

A low-speed camera is put on one side of the sandstone to record the surface changes in the sandstone during the experiment, which will be triggered when the experimental equipment starts working. A high-speed camera is put on the other side of the sandstone to record the surface deformations of the sandstone before and after the moment of failure. The optical axes of the two cameras are placed perpendicular to the surface of the specimen at the same time. When the sandstone is damaged the high-speed camera will be triggered, and 5750 images will be saved in total. The high-speed camera will save the specimen deformation images 7.5 s before and 4 s after the damage occurred; that is, 3750 frames before the damage and 2000 frames after the damage occurred. The placement of experimental instruments is shown in Figure 2.

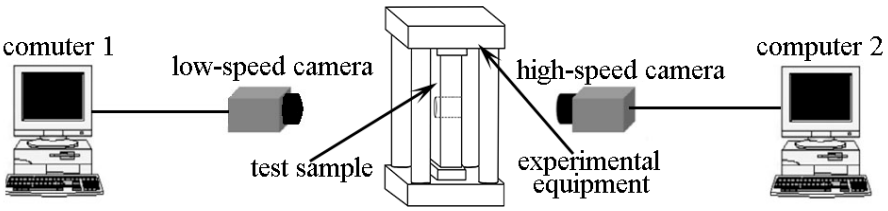

Figure 2. Schematic diagram of camera placement.

2.1. Speckle Preparation and Assessment

The basic process of DIC is described as follows: The camera records two speckle images before and after deformation of a measured object, and the corresponding two digital speckle gray fields are obtained by A/D conversion. A/D conversion is a way of converting an analog signal to a digital signal. Here, A/D conversion refers to the image of the visual signal into a digital signal, which is a gray-scale value. Correlation scanning and operations are performed on the two digital speckle images to find the point with a maximum the correlation coefficient, to obtain the relevant displacement information [16]. Generally, for an ideal speckle pattern, diameters of speckle points in an image should be ranged from 3 pixels to 5 pixels. The low-speed camera used in this experiment is TRUST DC 1600 with image resolution of 1626 pixels × 1236 pixels and focal length of camera lens is 12.5 mm. The high-speed camera used in this experiment was IX Cameras i-speed 221 with image resolution of 1616 pixels × 1706 pixels, and focal length of its lens is 25 mm. The sandstone sample size was 500 mm × 500 mm. In this paper, random black spot-like speckles with a diameter of 1–2 mm are made by a marker pen with the sandstone's primary color as the background. The speckle pattern is shown in Figure 3.

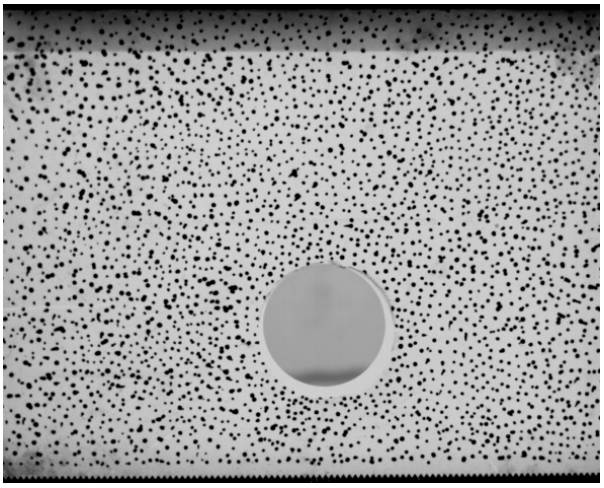

Figure 3. Speckle pattern of the sandstone sample.

Among the current speckle evaluation parameters, the Mean Intensity Gradient (MIG) proposed by Pan [17], the Mean Intensity of the Second Derivative (MISD) proposed by Yu [18], and the Shannon Entropy (SE) proposed by Liu [19] are the three most widely used evaluation criteria. The formula of the MIG (represented by δ_f) is shown in Equation (1):

$$\delta_f = \frac{\sum_{i=1}^{W}\sum_{j=1}^{H}\left|\nabla f(x_{ij})\right|}{W \times H} \tag{1}$$

In Equation (1), W and H are the width and height of the image (in pixels); $\left|\nabla f(x_{ij})\right| = \sqrt{f_x(x_{ij})^2 + f_y(x_{ij})^2}$ is the modulus of gray gradient vector at pixel x_{ij}; $f_x(x_{ij})$, and $f_y(x_{ij})$ are the gray-scale derivatives of pixel x_{ij} in x and y directions, respectively. We adopted Roberts cross gradient operator to replace gray-scale derivatives in two directions, and its formula is Equation (2):

$$\begin{cases} f_x(x_{ij}) = f(i,j) - f(i+1,\ j+1) \\ f_y(x_{ij}) = f(i,j+1) - f(i+1,\ j) \end{cases} \tag{2}$$

Pan [17] proposed that a larger MIG of speckle images has a smaller the mean bias error (u_e) and standard deviation (σ_u). Two error calculation formulas are Equations (3) and (4):

$$u_e = u_{mean} - u_{imp} \tag{3}$$

$$\sigma_u = \sqrt{\frac{1}{n-1}\sum_{i=1}^{n}\left(u_{mean} - u_{imp}\right)^2} \tag{4}$$

In Equations (3) and (4), $u_{mean} = \frac{1}{n}\sum_{i=1}^{n} u_i$ is the arithmetic mean value of n point displacement calculation results; u_{imp} is pre-added real sub-pixel displacement. Yu [18] proposed that the MISD (represented by ω_f) can be used to compare the speckle quality when the MIG is not different enough to intuitively reflect the quality of two speckle patterns. For speckle patterns with almost the same MIG, the smaller MISD it has, the smaller the displacement measurement error. The formula of MISD is Equation (5):

$$\omega_f = \frac{\sum_{i=1}^{W}\sum_{j=1}^{H}\left|\nabla^2 f(x_{ij})\right|}{W \times H} \tag{5}$$

In this equation, $\left|\nabla^2 f(x_{ij})\right| = \sqrt{f_{xx}(x_{ij})^2 + f_{yy}(x_{ij})^2}$ is the vector mode of the second derivative of the gray level of each pixel; $f_{xx}(x_{ij})$ and $f_{yy}(x_{ij})$ are the second derivative of the gray-scale value of pixel x_{ij} in the x and y directions, which can be used to substitute calculation by second order difference shown in Equation (6):

$$\begin{cases} f_{xx}(x_{ij}) = f(i,\ j-1) - 2f(i,\ j) + f(i,\ j+1) \\ f_{yy}(x_{ij}) = f(i-1,j) - 2f(i,\ j) + f(i+1,\ j) \end{cases} \tag{6}$$

SE (Shannon entropy), proposed by Shannon in 1948, is an indicator to measure the uncertainty related to random variables in information theory. According to the basic concept, Liu [19] used it in the DIC field to evaluate the quality of speckle pattern. For a

speckle pattern, the larger the SE (represented by δ_s) it has, the smaller the measurement error. SE formula is shown by Equation (7):

$$\delta_s = \sum_{i=0}^{2^\beta - 1} p(a_i) \log(p(a_i)) \tag{7}$$

In this equation, β is the pixel gray-scale depth of the image (8-bit images are used in practical operation, so i ranges from 0 to 255, which can be regarded as gray-scale values); $p(a_i)$ is the probability of occurrence of each gray-scale level.

The first picture from the low-speed camera in this experiment (shown in Figure 4A), and the first picture from the high-speed camera (see Figure 4B) are used to assess the speckles' quality. Meanwhile, the surface of a standard sample is randomly sprayed with black and white paint. Altogether, 1000 images from a low-speed camera (TRUST DC 1600) are used in this experiment, and their average (see Figure 4C) and one random image (see Figure 4D) are taken for comparison. Cut these three images into the same size (1566 pixel × 1166 pixel), and then perform relevant operations on their gray-scale values according to the above Equations (1), (5) and (7). MIG, MISD and SE are shown in Table 1.

Table 1. MIG, MISD and SE of four speckle patterns.

Speckle Pattern	MIG	MISD	SE
A	17.2696	15.3053	9.8501
B	19.9866	16.4400	7.1012
C	23.2605	21.7038	11.4230
D	22.1941	20.6816	11.3406

As shown in Table 1, the MIG of speckle pattern A and B in this experiment is smaller than that of speckle pattern C and D, which is randomly sprayed and averaged. The causes are concluded as follows: (1) speckle patterns C and D are taken in the laboratory statically, while speckle patterns A and B are taken in the experiment site; there is more noise in pattern A and B than C and D; (2) there are no speckles on the prefabricated hole in the center of speckle pattern A and B; (3) speckles in this experiment are randomly painted by marker pen, and the gray-scale values of the speckles were all close to 0. Speckles in speckle patterns C and D are made by spraying, and their gray-scale values did not appear in the above situation. That is the reason why the gray-scale values of speckle pattern A and B are small in the above numerical calculation. Because the size of the specimen is large in this experiment, it is too difficult to make suitable spots by spraying because speckle spots are bound to be too small. Therefore, a 1 mm marker pen is used to randomly paint speckle on the surface of the specimen (500 mm × 500 mm). In the case of a low-speed camera with image resolution of 1626 pixel × 1236 pixel and a high-speed camera with image resolution of 1616 pixel × 1706 pixel, the diameter of speckle spots could be 3–5 pixels.

2.2. Compression Experiment

The experiment system is shown in Figure 5. The sandstone was placed on the experimental equipment. To ensure the uniform force of the specimen, two steel plates are placed on the top and bottom of the sandstone. The length, width and thickness of the steel plate are 800 mm × 300 mm × 30 mm. The upper and lower surfaces of the sandstone are evenly coated with petroleum jelly to reduce the influence of friction. The center of the vertical compression column and the center of the specimen are adjusted to a vertical line to prevent eccentric compression. The confining pressure of 3 MPa is added on the left and right sides of the sandstone; on the one hand, to simulate a more realistic cavern environment, and on the other hand, to prevent the sandstone from being damaged too quickly. Although, it is well known that the stress state in the real tunnel is close to a triaxial state. In fact, from the experimental point of view, the failure forms of the sandstone under the action of triaxial state and biaxial state are not different [20]. At

the same time, considering that DIC equipment is required in this experiment, therefore, we finally chose to carry out this biaxial loading mode in this experiment. Two cameras are fixed on the front and rear sides of the sandstone, and the position, focal length and lighting equipment (white light source) of the two cameras are adjusted according to the experimental environment.

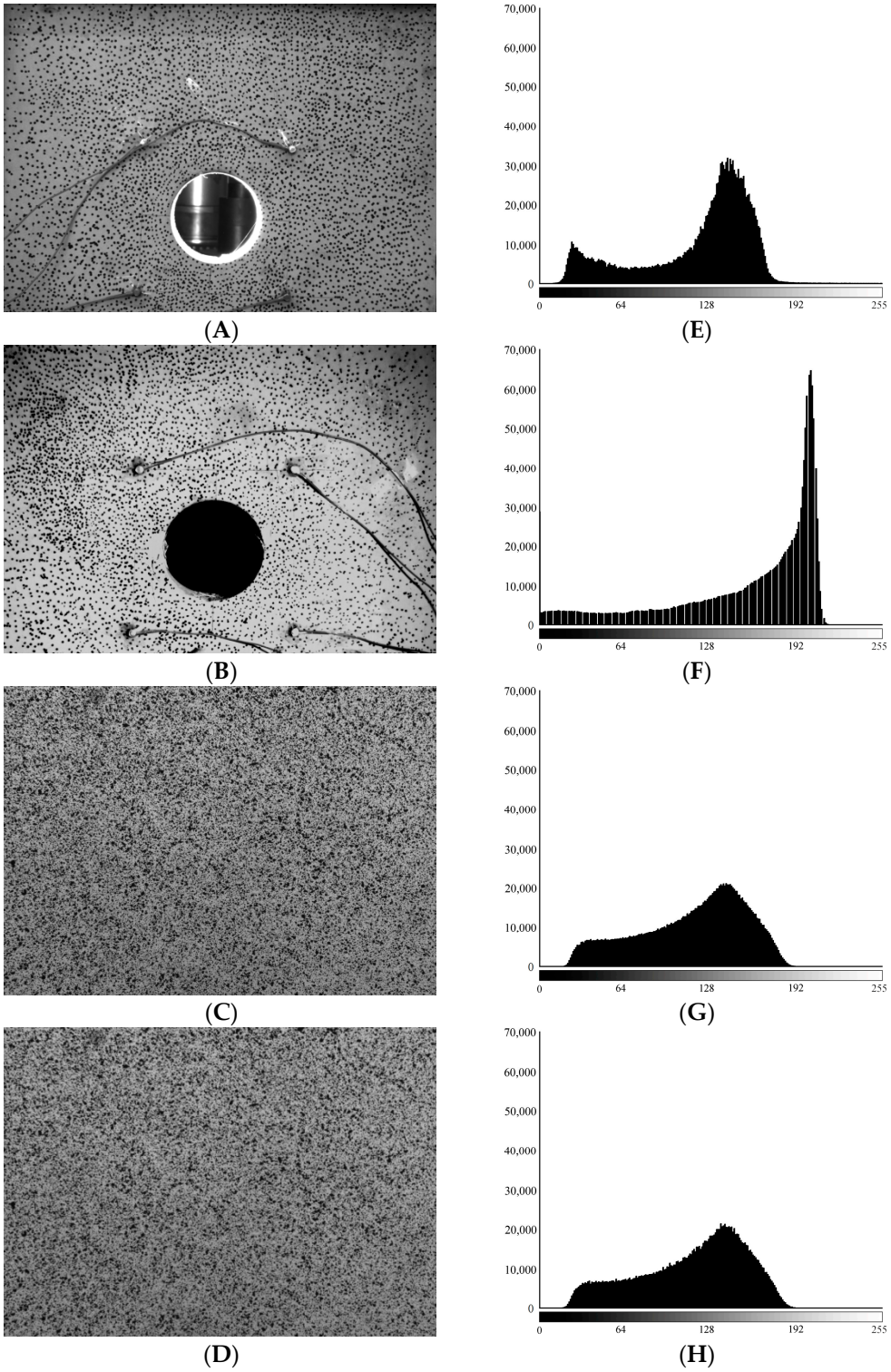

Figure 4. Speckle pattern (**A**–**D**) and their gray-scale histogram (**E**–**H**).

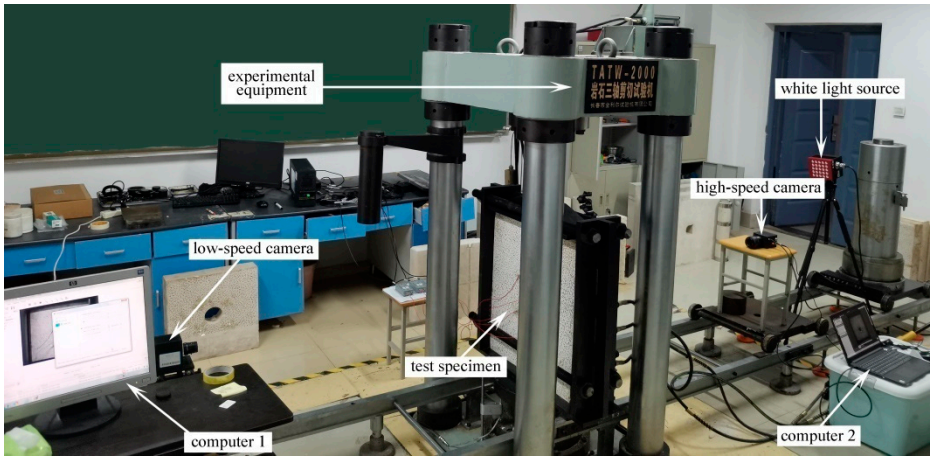

Figure 5. Experiment system.

After that, multistage velocity loading is used to compress the specimen. At the start of loading, both cameras started recording speckle patterns simultaneously. The low-speed camera records images at the rate of 1 frame/s, and the high-speed camera gets images at the rate of 500 frames/s (at this time, those images collected by the high-speed camera are not saved). The low-speed camera uses the VIC-Snap acquisition system, while the high-speed camera uses the IX-2 series acquisition system. The experimental equipment and two cameras are stopped simultaneously when the specimen is damaged. At this point, the low-speed camera stopped completely, and the images were saved to the computer. The high-speed camera saved the images taken in the last 11.5 s (determined by the selected high-speed camera). We selected the images taken 7.5 s before and 4 s after the failure to observe the instantaneous changes in the sandstone surface when the failure appears. It can also record the change in the location and depth of the crack, peel and other failure parameters. Finally, DIC analysis software VIC-2D (produced by the American company Correlated Solutions, Irmo, SC, USA) was used to analyze and calculate the collected speckle pattern, to obtain the displacement field and strain field of the sandstone during the experiment.

The stress–strain curve in Figure 6 is drawn to reflect the loading mode of the sandstone. The stress and strain data are calculated from the data obtained by the experimental equipment's sensor.

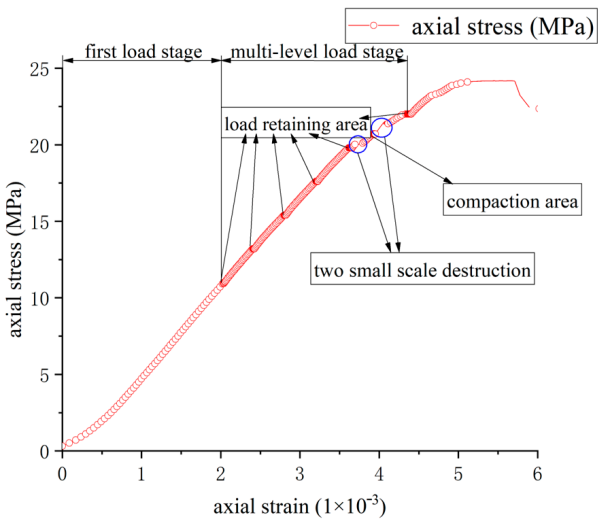

Figure 6. Stress–strain curve of whole experiment process.

To save on the experiment time and collect more data at each level of compression, the multi-level speed compression method was used in the experiment. Firstly, load control was used to increase the pressure of the experimental equipment to 550 kN (axial strain 11 MPa) at the rate of 500 N/s and keep the load for 300 s. According to the previous experiment results, the ultimate compression that the specimen could bear is about 1100 kN, so 550 kN was selected to load about 50% of the peak compression at the first stage.

The compression speed is 0.02 mm/min. The compression increment of each stage is about 10% of the peak compression (110 kN). After loading at each stage, the load is kept for 300 s until the test was stopped after the failure of sandstone. The relevant sparse curve is shown in Figure 6. When the pressure of the experimental equipment is loaded to 550 kN (axial stress 11 MPa), the points on the stress–strain curve are dense due to changes in the loading mode, because the speed of successive loading is slower than that of the first stage. After the completion of primary loading there will be a section of more dense area, namely the load retaining area. At the same time, it is not difficult to find from the stress–strain curve during the experiment that during the first five stages of loading the stress and strain are almost proportional; that is, the sandstone is in the elastic stage. There are no obvious macroscopic cracks on the specimen surface at the elastic stage. When the experimental equipment was loaded to 1001 kN (axial strain was about 20 MPa, 82.8% of the peak compression), a small range of stress release occurred in the sandstone, and obvious macroscopic cracks appeared on the sandstone surface. However, as the loading continued these cracks did not continue to expand but were compacted with the increase in pressure. The stress–strain curve reflects a break point, followed by a point dense compaction area (at this time, the experimental equipment loading pressure is about 1035 kN, and the axial strain is about 20.7 MPa). After a period of compaction, a small range of stress release occurred again because the experimental equipment kept pressing down at a speed of 0.02 mm/min. Soon after the failure, the sixth load protection area (the experimental equipment loading pressure is about 1100 kN) is entered, and the compaction area of those cracks overlapped with the load retaining area. Due to the peak axial load, this sandstone reached 24.18 MPa (the experimental equipment loading peak pressure is about 1209 kN). After the sixth load protection area the experimental equipment continued to be pressurized until the sandstone was failed completely.

3. Results Analyses

A total of 11,940 pictures were taken in this group, of which 6190 were taken by low-speed camera to record the whole process of the experiment. The high-speed camera took 5750 images and records the changes in the specimen 7.5 s before and 4 s after the final failure.

3.1. Analysis on the Images Taken by Low-Speed Camera

During the experiment, the digital image acquisition system recorded the speckle patterns on the sandstone surface. In this paper, the VIC-2D software of Correlated Solutions was used for image processing. The analysis on the images taken by the low-speed camera was as follows: DIC analysis software took the first image as the reference image during calculation to obtain the displacement field of the whole destruct process firstly. Then, the VIC-2D software can finally obtain the Lagrange finite strain by calculating the deformation gradient tensor. Eight typical moments in the whole experiment process were selected as follows: In the 1100 s, the first load stage was complete and the sandstone has just entered the first load retaining area; in the 2000 s, the second-level loading was finished and the sandstone entered the second load retaining area; in the 2800 s, the third-level loading was finished and the sandstone entered the third load retaining area; in the 3700 s, the fourth-level loading was finished and the sandstone entered the fourth load retaining area; in the 4500 s, the fifth-level loading was finished and the sandstone entered the fifth load retaining area; in the 5015 s, the first small range of stress release just ended, and the sandstone entered the first compaction area; in the 5400 s, the second small range of

stress release just ended and the sandstone entered the last load retaining area, namely the second compaction area. In the 6179 s the experimental equipment reached the peak pressure (1209 kN), and the sandstone was about to be destroyed. The evolution diagram of displacement field and strain field at eight moments is shown in Figures 7 and 8.

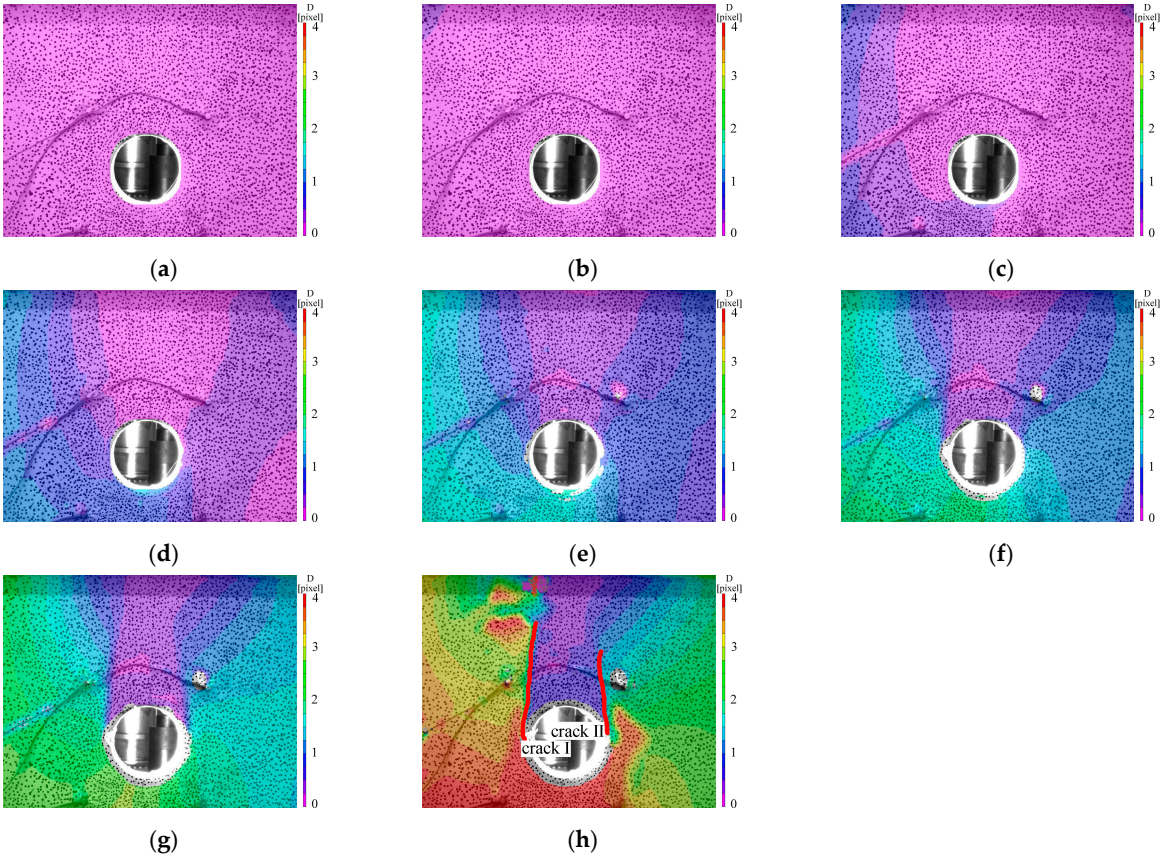

Figure 7. Variations in displacement field. The unit of displacement in this figure is pixel. (**a**) t = 1100 s, F = 549.34 kN. (**b**) t = 2000 s, F = 660.02 kN. (**c**) t = 2800 s, F = 770 kN. (**d**) t = 3700 s, F = 879.99 kN. (**e**) t = 4500 s, F = 990.01 kN. (**f**) t = 5015 s, F = 1035.13 kN. (**g**) t = 5400 s, F = 1100 kN. (**h**) t = 6179 s, F = 1208.9 kN.

According to the result of displacement analysis, before the final failure, some macroscopic cracks appeared on the sandstone surface due to the stress release in two small ranges of stress release. Among all cracks, there are two most obvious cracks that appeared on the left and right sides above the prefabricated hole (crack I and II shown in Figure 8). In the middle of two cracks, that is, just above the prefabricated hole, the displacement was obviously smaller than the other positions. There was an obvious displacement difference on both sides of the crack I and crack II. As shown in Figure 7, the displacement on the left side of crack I was almost parallel to the crack I, while the displacement on the right side of crack I had a certain angle with that of crack I. Therefore, crack I was not a simple opening mode crack or sliding mode crack, but rather a coupling of the two. The displacements on both sides of crack II were almost in the same direction and there was a certain angle with crack II, so crack II was more like an opening mode crack. As shown in Figure 7, the displacement distribution on the left and right sides of the prefabricated hole shows a certain symmetry, which indicates that the specimen was well prepared and uniformly loaded and met the expected results. In addition, it can also be seen that there was no obvious deformation on the sandstone surface before 5000 seconds (that is, before two small ranges of stress release). Therefore, the analysis of the strain before 5000 seconds is not performed anymore.

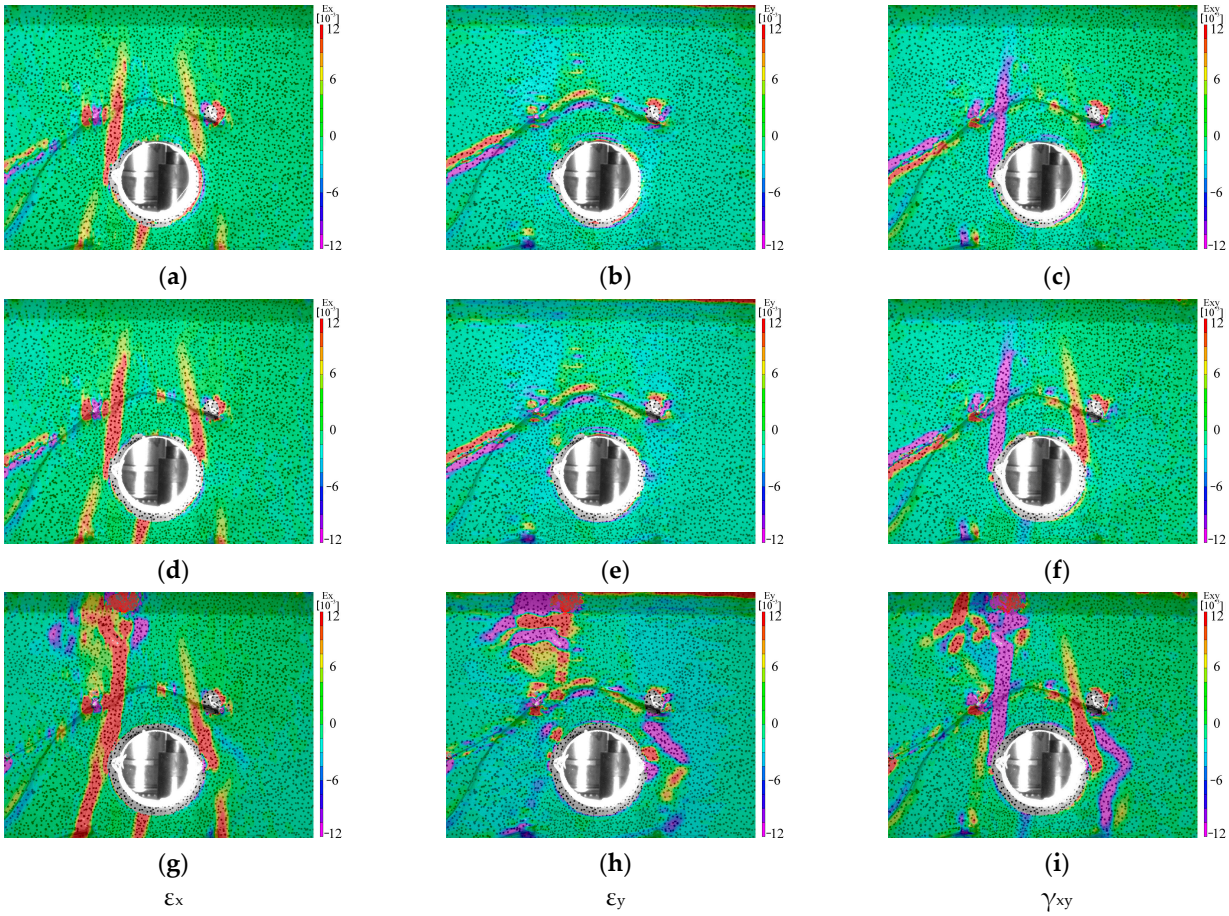

Figure 8. Strain in x-direction (ε_x), y-direction (ε_y) and shear (γ_{xy}). Where (**a**–**c**) are at time t = 5015 s, when F = 1035.13 kN. (**d**–**f**) are at time t = 5400 s, when F = 1100 kN. (**g**–**i**) are at time t = 6179 s, when F = 1208.9 kN.

Obvious stress concentration around cracks I and II is as shown in Figure 7h. The y-directional stress σ_y around the two cracks is not obvious. We know that new stress equilibrium will be sought after a crack occurs. If a new equilibrium point is found, the crack remains at a "plateau" for some time. After the new stress equilibrium is broken again, the crack will spread further. If the stress equilibrium point is not found or the equilibrium is broken again, the crack will continue to expand. At the same time, even stripping, fragmentation, rock ejection and other damage will appear. Therefore, the stress around crack I does not change significantly from t = 5015 s to t = 5400 s. However, crack II appeared at about t = 5315 s and rapidly expanded within a few seconds. When t = 5400 s, crack II stopped expanding. According to the strain diagram, the x-directional stress σ_x on both sides of crack II increased from t = 5015 s to t = 5400 s, but not significantly. However, when t = 5015 s there was no significant shear stress τ_{xy} on both sides of the crack II, while when t = 5400 s there was already a significantly larger shear stress τ_{xy} on both sides of the crack II. Therefore, crack II was mainly caused by normal stress, which is consistent with the characteristics of opening mode crack.

3.2. Analysis on the Images Taken by High-Speed Camera

Due to a large quantity image recorded by high-speed cameras per second (1 s can save 500 frames), the high-speed camera cannot be used to record the whole experiment process (about 2 h). The high-speed camera can only be used to record the changes in the sandstone surface before and after the failure. In this experiment, the high-speed camera was used to record the surface state of the sandstone 7.5 seconds before and 4 seconds

after the failure. However, when processing the images taken by high-speed cameras, it is impossible to take the surface state of sandstone before the experiment. When processing images taken by the high-speed camera (t = 6171.8 s) it is impossible to take the surface state of specimen before the experiment as the reference for DIC analysis of subsequent images. Therefore, the early displacement and strain of the images recorded by the high-speed camera are small. We selected two cracks, III and IV, that appear in two small ranges of stress release for analysis, as shown in Figure 9. (Note: Crack III and crack I were two cracks, rather than the same through-crack).

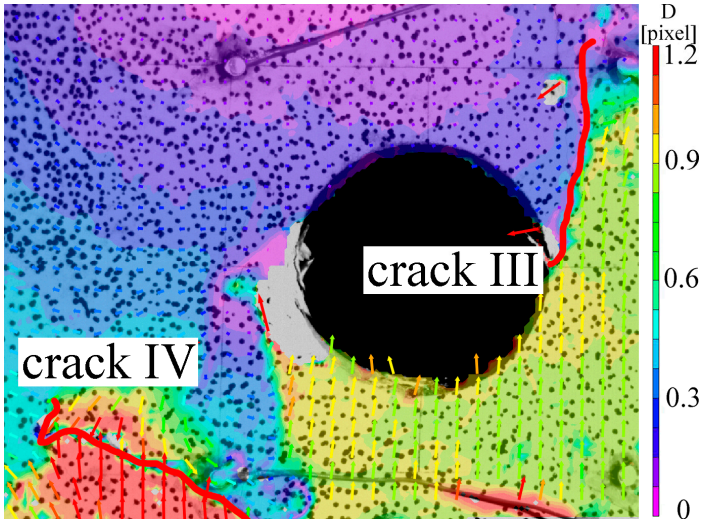

Figure 9. Displacement of specimen surface captured by high-speed camera at t = 6179 s. The unit of displacement in this figure is pixel.

As shown in Figure 10, when t = 6175.3 s the strain around cracks III and IV did not change compared with the strain around cracks at t = 6171.8 s. However, when t = 6178.9 s, crack III and IV on both sides of the strain increased greater than t = 6171.8 s. In fact, stress concentration has appeared around the crack III and IV at t = 6171.8 s. With the continuous pressure of the testing machine, both the stress and stress intensity factor K around the crack III and IV increased. When t = 6179 s the crack IV firstly broke the original equilibrium and began to expand. Within 0.02 seconds, the crack IV rapidly expanded to about twice the original length and the direction changed from the original transverse to longitudinal. However, crack III did not expand further until the end. It shows that not all the macroscopic cracks or microcosmic cracks which appeared before will expand when the final failure occurs. When t = 6179 s a strip stress concentration area appeared above the right end of the prefabricated hole. If the sandstone is not damaged soon and the stress is released in other areas, a crack should also appear in this area. Thus, it can be seen that the cracks parallel to the direction of the applied load are easy to appear when the prefabricated holes are perpendicular to both ends of the direction of the applied load.

According to comprehensive analysis result of strain changes on both sides of the sandstone, it is not difficult to discover that the distribution of normal stress concentration area and shear stress concentration area were almost the same at the late compression stage (t > 5400 s). This indicates that both the macroscopic cracks and the crack-prone areas were subjected to the normal stress–shear stress coupling effect at the late stage of compression.

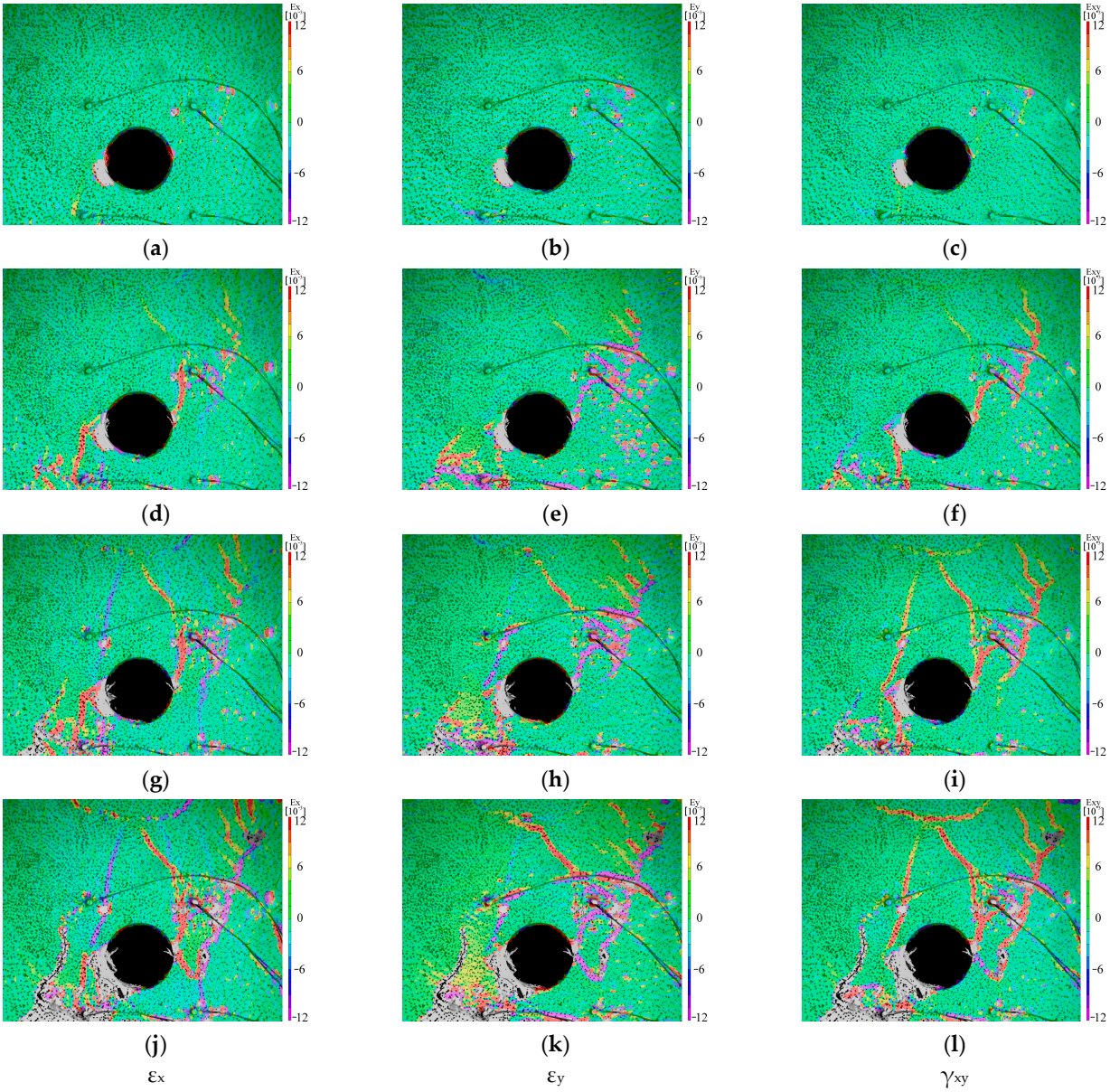

Figure 10. Strain in x-direction (ε_x), y-direction (ε_y) and shear (γ_{xy}). Where (**a**–**c**) are at time t = 6175.3 s, when F = 1208.27 kN. (**d**–**f**) are at time t = 6178.9 s, when F = 1208.87 kN. (**g**–**i**) are at time t = 6179 s, when F = 1208.9 kN, (**j**–**l**) are at time t = 6179.02 s, when F = 1208.87 kN.

Comparing the development of cracks in multiple groups sandstone when they were finally destroyed is shown in Figure 11. We can find that there is an obvious gap in the displacement above the prefabricated hole, and cracks are easy to occur where the displacement difference is too large. The concentration of shear stress and x-direction stress also appears in these areas, which is consistent with the displacement change rules and the conclusions of the previously analyzed specimens.

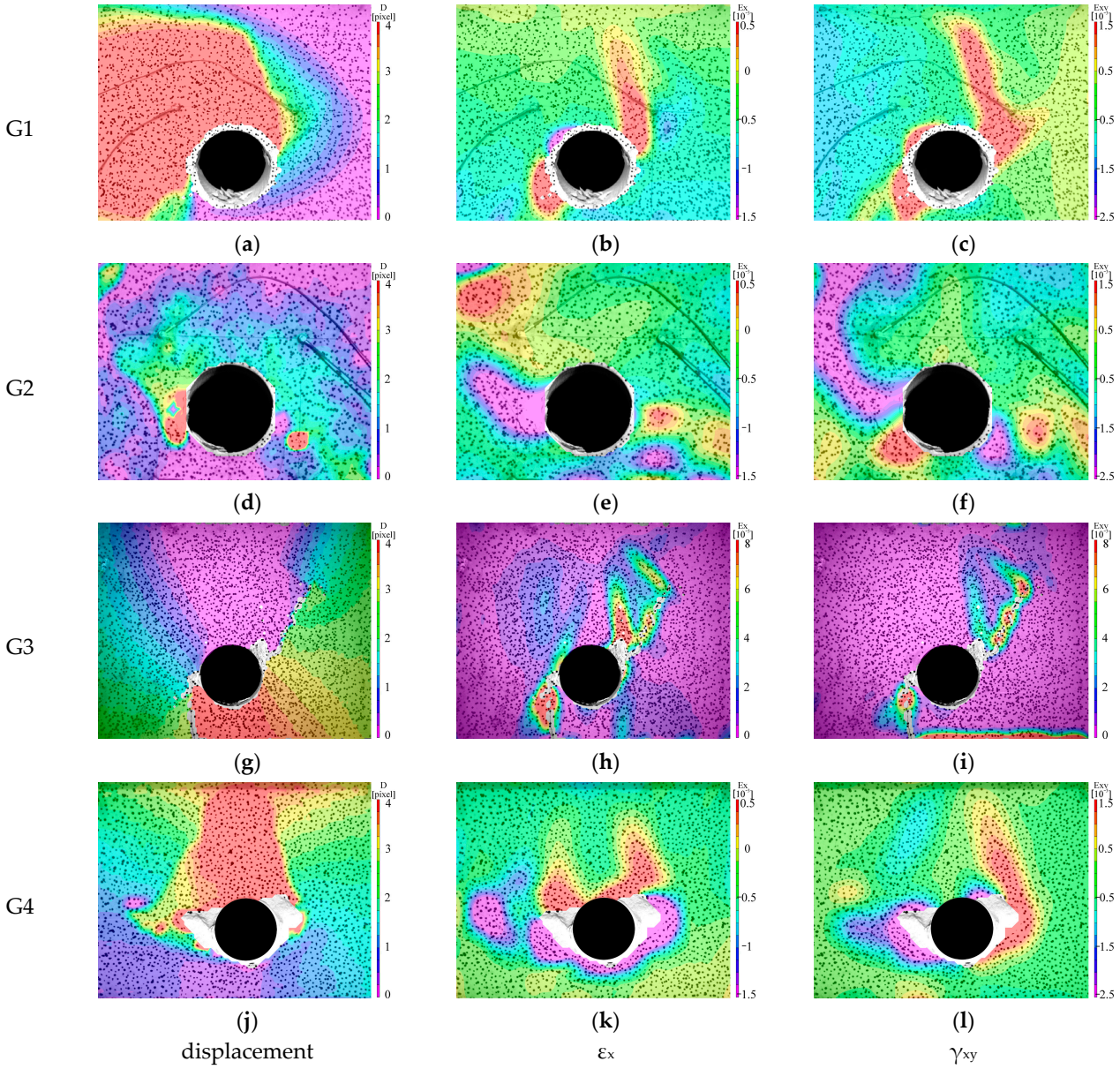

Figure 11. Displacement, x-directional strain (ε_x) and shear strain (γ_{xy}) of multiple groups sandstone specimens. When these groups specimens G1, G2, G3, G4 were destroyed, they were captured by the low-speed camera. The results of each group displacement, ε_x and γ_{xy} are given. Where (**a**–**c**) belongs to group G1, which is destroyed at t = 6275 s and F = 1198 kN, (**d**–**f**) belongs to group G2, which is destroyed at t = 5503 s and F = 1105 kN, (**g**–**i**) belongs to group G3, which is destroyed at t = 6105 s and F = 1210 kN, (**j**–**l**) belongs to group G4, which is destroyed at t = 5905 s and F = 1111 kN.

4. Conclusions

We studied the compression process of large sandstone with a prefabricated hole by a dual DIC system and assessed the quality of the fabrication of speckle on specimen surface. The conclusions are listed as follows:

(1) To get suitable speckles on the surface of the large rock specimen, we used marker pen dots to create speckles, to keep the size of the individual speckle point diameter between 3 and 5 pixels. The multi-angle monitoring of the whole process of deformation and instantaneous failure is realized, and the measurement results are effectively analyzed;

(2) In the compression process of the sandstone with a prefabricated hole, the specimen was always in the elastic stage before and during the middle stage of compression (before

the pressure of the experimental equipment reached about 80% of the peak pressure), and no obvious macroscopic cracks appeared on its surface. As the load increased, the sandstone had several small stress releases and several obvious macroscopic cracks. However, if the whole sandstone does not reach the yield limit, there will be no final failure. In addition, the macroscopic cracks that appeared before will stabilize after finding a new "equilibrium point";

(3) At the late stage of loading, the distribution of normal stress concentration area and shear stress concentration area were almost coincident, and the macroscopic cracks and crack-prone area were affected by the normal stress–shear stress coupling effect;

(4) It is easy to appear I (opening mode crack) or II (sliding mode crack) type cracks parallel to the direction of the applied load when the prefabricated holes are perpendicular to both ends of the direction of the applied load. This area was the "Frequent area" of cracks. The deformation rock burst features such as stripping, fragmentation and rock ejection appeared around the prefabricated hole when the final failure occurred.

Author Contributions: Conceptualization, F.C. and L.Z.; methodology, F.C. and Y.Z.; software, F.C.; validation, X.G. and Y.Z.; formal analysis, F.C., Z.G., J.S., Y.W. and Y.L.; investigation, L.Z.; resources, F.C.; data curation, Y.Z., F.C. and X.G.; writing—original draft preparation, F.C. and Y.Z.; writing—review and editing, F.C.; visualization, F.C.; supervision, F.C. and C.L.; project administration, F.C.; funding acquisition, F.C. All authors have read and agreed to the published version of the manuscript.

Funding: This research was funded by [National Natural Science Foundation of China] Grant Numbers [12072170] and grant number [11472145], Department of Education of Shandong Province [Special fund for Taishan Scholars Project] grant number [tsqn202211180], [Team development plan of young and innovative talents introduction and education plan in Colleges and universities of Shandong Province] grant number [2019-039].

Institutional Review Board Statement: The study was not involving humans or animals.

Informed Consent Statement: The study was not involving humans.

Data Availability Statement: The datasets generated during or analyzed during the current study are available from the corresponding author on reasonable request.

Acknowledgments: Thanks for the support of Department of Education of Shandong Province "Special fund for Taishan Scholars Project" and "Team development plan of young and innovative talents introduction and education plan in Colleges and universities of Shandong Province (2019-039)" hosted by Fanxiu Chen.

Conflicts of Interest: The authors declare no conflict of interest.

References

1. Tian, M.; Han, L.; Meng, Q.; Ma, C.; Zong, Y.; Mao, P. Physical model experiment of surrounding rock failure mechanism for the roadway under deviatoric pressure form mining disturbance. *KSCE J. Civ. Eng.* **2020**, *24*, 1103–1115. [CrossRef]
2. Jiang, M.; Sima, J.; Cui, Y.; Hu, H.; Zhou, C.; Lei, H. Experimental investigation of the deformation characteristics of natural loess under the stress paths in shield tunnel excavation. *Int. J. Geomech.* **2017**, *17*, 04017079. [CrossRef]
3. Li, T.; Yang, X. Probabilistic stability analysis of subway tunnels combining multiple failure mechanisms and response surface method. *Int. J. Geomech.* **2018**, *18*, 04018167. [CrossRef]
4. Xu, Y.; Dai, F. Dynamic response and failure mechanism of brittle rocks under combined compression-shear loading experiments. *Rock Mech. Rock Eng.* **2018**, *51*, 747–764. [CrossRef]
5. Zhou, Z.; Cai, X.; Li, X.; Cao, W.; Du, X. Dynamic response and energy evolution of sandstone under coupled static-dynamic compression: Insights from experimental study into deep rock engineering applications. *Rock Mech. Rock Eng.* **2020**, *53*, 1305–1331. [CrossRef]
6. Wang, Y.; Zhang, H.; Lin, H.; Zhao, Y.; Liu, Y. Fracture behaviour of central-flawed rock plate under uniaxial compression. *Theor. Appl. Fract. Mech.* **2020**, *106*, 102503. [CrossRef]
7. Huang, Y.; Yang, S. Mechanical and cracking behavior of granite containing two coplanar flaws under conventional triaxial compression. *Int. J. Damage Mech.* **2019**, *28*, 590–610. [CrossRef]
8. Duan, Y.; Li, X.; Zheng, B.; He, J.; Hao, J. Cracking evolution and failure characteristics of Longmaxi shale under uniaxial compression using real-time computed tomography scanning. *Rock Mech. Rock Eng.* **2019**, *52*, 3003–3015. [CrossRef]

9. Dai, S.; Gao, W.; Wang, C.; Xiao, T. Damage evolution of heterogeneous rocks under uniaxial compression based on distinct element method. *Rock Mech. Rock Eng.* **2019**, *52*, 2631–2647. [CrossRef]
10. Zhao, J.; Feng, X.; Zhang, X.; Zhang, Y.; Zhou, Y. Brittle-ductile transition and failure mechanism of Jinping marble under true triaxial compression. *Eng. Geol.* **2018**, *232*, 160–170. [CrossRef]
11. Gao, Y.; Feng, X.; Zhang, X.; Feng, G.; Jiang, Q.; Qiu, S. Characteristic stress levels and brittle fracturing of hard rocks subjected to true triaxial compression with low minimum principal stress. *Rock Mech. Rock Eng.* **2018**, *51*, 3681–3697. [CrossRef]
12. Yamaguchi, I. A laser-speckle strain gauge. *J. Phys. E Sci. Instrum.* **1981**, *14*, 1270–1273. [CrossRef]
13. Peters, W.H.; Ranson, W.F. Digital Imaging Techniques in Experimental Stress Analysis. *Opt. Eng.* **1981**, *21*, 427–431. [CrossRef]
14. Chen, F.; Zhuang, Q.; Zhang, H. Mechanical analysis and force chain determination in granular materials using digital image correlation. *Appl. Opt.* **2016**, *55*, 4776–4783. [CrossRef] [PubMed]
15. Liu, L.; Li, H.; Li, X.; Wu, D.; Zhang, G. Underlying mechanisms of crack initiation for granitic rocks containing a single pre-existing flaw: Insights from digital image correlation (DIC) analysis. *Rock Mech. Rock Eng.* **2021**, *54*, 857–873. [CrossRef]
16. Chen, F.; Zhuang, Q.; Wang, R.; Guo, P. Damage point prediction of a force chain based on digital image correlation method. *Appl. Opt.* **2017**, *56*, 636–643. [CrossRef] [PubMed]
17. Pan, B.; Lu, Z.; Xie, H. Mean intensity gradient: An effective global parameter for quality assessment of the speckle patterns used in digital image correlation. *Opt. Lasers Eng.* **2010**, *48*, 469–477. [CrossRef]
18. Yu, H.; Guo, R.; Xia, H.; Yan, F.; Zhang, Y.; He, T. Application of the mean intensity of the second derivative in evaluating the speckle patterns in digital image correlation. *Opt. Lasers Eng.* **2014**, *60*, 32–37. [CrossRef]
19. Liu, X.; Li, R.; Zhao, H.; Cheng, T.; Cui, G. Quality assessment of speckle patterns for digital image correlation by Shannon entropy. *Opt. Int. J. Light Electron Opt.* **2015**, *126*, 4206–4211. [CrossRef]
20. Zhang, L.; Cong, Y.; Meng, F.; Wang, Z.; Zhang, P.; Gao, S. Energy evolution analysis and failure criteria for rock under different stress paths. *Acta Geotech.* **2021**, *16*, 569–580. [CrossRef]